Journal of Materials Chemistry A

CO oxidation on $MgAl_2O_4$ supported Ir_n: Activation of lattice oxygen in the subnanometer regime and emergence of nuclearity-activity volcano

Journal:	*Journal of Materials Chemistry A*
Manuscript ID	TA-ART-11-2021-009740.R1
Article Type:	Paper
Date Submitted by the Author:	14-Jan-2022
Complete List of Authors:	Lu, Yubing; Virginia Polytechnic Institute and State University, Thompson, Coogan; Virginia Polytechnic and State University, Chemical Engineering Kuo, Chun-Te; Virginia Polytechnic and State University, Chemical Engineering Zhang, Xiwen; Virginia Polytechnic and State University, Chemical Engineering Hoffman, Adam; SLAC National Accelerator Laboratory, SSRL Boubnov, Alexey; Karlsruhe Institute of Technology, Bare, Simon; Stanford Linear Accelerator Center, SSRL Kovarik, Libor; Pacific Northwest National Laboratory, EMSL Xin, Hongliang ; Virginia Tech, Chemical Engineering; Virginia Tech Karim, A.; Virginia Polytechnic and State University, Chemical Engineering

ARTICLE

CO oxidation on $MgAl_2O_4$ supported Ir_n: Activation of lattice oxygen in the subnanometer regime and emergence of nuclearity-activity volcano

ƒReceived 00th January 20xx,
Accepted 00th January 20xx

DOI: 10.1039/x0xx00000x

Yubing Lu,‡[a] Coogan Thompson, ‡[a] Chun-Te Kuo,[a] Xiwen Zhang,[a] Adam S. Hoffman,[b] Alexey Boubnov,[b] Simon R. Bare,[b] Libor Kovarik,[c] Hongliang Xin,[a] Ayman M. Karim*[a]

CO oxidation on Pt group metals is affected by the metal size and reducibility of the oxide support. Here, we report that Ir supported on $MgAl_2O_4$, traditionally considered non-reducible, exhibits properties similar to reducible oxides when the Ir size is in the subnanometer regime. To show this effect, we synthesized subnanometer Ir clusters and compared their properties to single atoms and nanoparticles (1–1.5 nm). The CO oxidation activity is highest on $Ir_{0.6\text{-}0.8nm}$ while showing distinctly different reaction orders in CO and O_2, (0, +0.4) than single atoms (1, 0) and nanoparticles (−1, +1). Microcalorimetry, *in-situ* X-ray absorption and infrared spectroscopies show that the CO-saturated $Ir_{0.6\text{-}0.8nm}$ clusters could adsorb and activate O_2 despite binding CO more strongly than nanoparticles. Density functional theory calculations on CO saturated Ir_4 clusters suggest that the increased activity is due to the ability to activate O_2 on oxygen vacancies at the Ir-$MgAl_2O_4$ interface. The findings show the important effect of the metal nuclearity on the support and catalyst properties and can guide future design of CO oxidation catalysts.

Introduction

Supported precious metal catalysts are used to perform many important chemical transformations. Dispersing the metals as single atoms and small clusters has become a common strategy to increase the percentage of atoms available for binding and transformation of the reactants.[1, 2] However, supported metal single atoms and subnanometer clusters typically have different reactivity compared with their nanoparticle counterparts.[3-6] As the metal nuclearity decreases into the subnanometer regime, the metal electronic properties can change substantially due to the lower number of neighboring metal atoms and enhanced interaction with the support.[7-9] The different properties of isolated atoms, dimers and subnanometer clusters can lead to different reaction mechanisms and/or improved reactivity (e.g. superior activity and/or selectivity)[10-15], but this is highly dependent on the reaction, the type of metal, and support. For low-temperature (< 200 °C) CO oxidation on platinum group metals, there are reports of both higher (e.g. Pt/FeO_x[15], Pt/mesoporous-Al_2O_3[16] Rh/CeO_2[17] and $Ir/MgAl_2O_4$[18, 19]) and lower (e.g. Pt/Al_2O_3[20] Pt/H-ZSM5[21], Pt/CeO_2[22, 23] and Rh/TiO_2[24]) activity on supported metal single atoms compared to nanoparticles. Additionally, the activity can be strongly dependent on metal nuclearity as shown for size selected Pd_n clusters (n=1–25) deposited on rutile TiO_2(110) where the activity was highest on Pd_{20}.[25] In this regard, understanding the effect of metal nuclearity on reactivity is important on a fundamental level and offers an opportunity to tune the metal properties and design highly active catalysts.

For low temperature CO oxidation on supported precious metals, the metal nuclearity and support strongly affect the adsorption of CO and O_2, the reaction mechanism, and the catalyst activity. O_2 activation is highly dependent on the type of the support. On non-reducible oxides (Al_2O_3, $MgAl_2O_4$, etc.), O_2 activation proceeds via the Langmuir–Hinshelwood (L–H) mechanism on the nanoparticles, and due to the strong CO adsorption on the metal and lack of adjacent sites for O_2 adsorption and activation, the activation proceeds on one empty metal site assisted by an adsorbed CO on an adjacent metal site.[26] On reducible metal oxides (e.g. CeO_2 and TiO_2), CO oxidation proceeds at the interface where CO on the metal nanoparticle reacts with O* at the metal/support interface.[23, 27-31] The metal support interaction also plays an important role in O_2 activation. For example, Oh et al. showed that the O_2 shows promoted activation on a defect site at the Pt-TiO_2 interface.[32] On the other hand, for single atoms on both reducible and non-reducible supports, most studies show that the support plays a crucial part in O_2 activation.[33-36] In the subnanometer regime, less is known about O_2 activation but it is likely size- and support-dependent. For example, Kaden et al. showed that Pd_{20}/TiO_2 can activate O_2 more efficiently than Pd_7/TiO_2 and

[a] *Department of Chemical Engineering, Virginia Polytechnic Institute and State University, Blacksburg, Virginia 24060, USA. Email: amkarim@vt.edu*
[b] *Stanford Synchrotron Radiation Light Source, SLAC National Accelerator Laboratory, Menlo Park, California 94025, USA.*
[c] *Institute for Integrated Catalysis, and Fundamental and Computational Science Directorate, Pacific Northwest National Laboratory, Richland, Washington 99354 USA.*

† Electronic Supplementary Information (ESI) available: size distribution of Ir samples, details of EXAFS modeling, details of reaction kinetic measurements, CO microcalorimetry results, DFT optimized structures. See DOI: 10.1039/x0xx00000x
‡ These authors contribute equally to this work.

Pd_4/TiO_2.[37] However, there are limited studies on the effect of metal nuclearity on CO oxidation in the subnanometer regime, especially on supports traditionally considered to be non-reducible.

Results and discussion

By combining advanced experimental and theoretical approaches including aberration-corrected transmission electron microscopy, microcalorimetry, *in-situ* and *operando* X-ray absorption (XAS), infrared spectroscopies, and density functional theory (DFT), we investigated the effect of Ir metal nuclearity on interaction with CO/O_2 and on the CO oxidation kinetics on $Ir/MgAl_2O_4$. We show that supported Ir subnanometer clusters are more active than single atoms and nanoparticles (>1 nm) and we attribute their superior activity to enhanced cooperation between the metal and support in the subnanometer regime. To achieve this, we synthesized a sample consisting of mostly Ir subnanometer clusters supported on $MgAl_2O_4$ (denoted as $Ir_{Subnano}/MgAl_2O_4$, Fig. 1b) and compared it with $MgAl_2O_4$ supported nanoparticles (denoted as $Ir_{NP}/MgAl_2O_4$, Fig. 1a) and single atoms (denoted as $Ir_{SA}/MgAl_2O_4$, Fig. 1c). Size analysis of multiple high angle annular dark field–scanning transmission electron microscopy (HAADF–STEM) images show that $Ir_{Subnano}/MgAl_2O_4$ contains mostly subnanometer clusters having an average cluster size of ~0.7 nm and ~28% of Ir is present as single atoms. HAADF-STEM characterization on the spent $Ir_{Subnano}/MgAl_2O_4$ confirmed the stability of the subnanometer Ir clusters under CO oxidation reaction conditions at 155 °C (Supplementary Information, Fig. S1 and Tables S1–S2). Powder X-ray diffraction spectroscopy (XRD) results (Supplementary Information Fig. S2) show that there were no significant changes to the support (MgAl2O4) structure due to the synthesis and that all species on the support were small as indicated by the lack of non-support peaks. This is consistent with the STEM, EXAFS, and chemisorption results indicating single atoms, subnanometer clusters, and small (1-2 nm) nanoparticles.

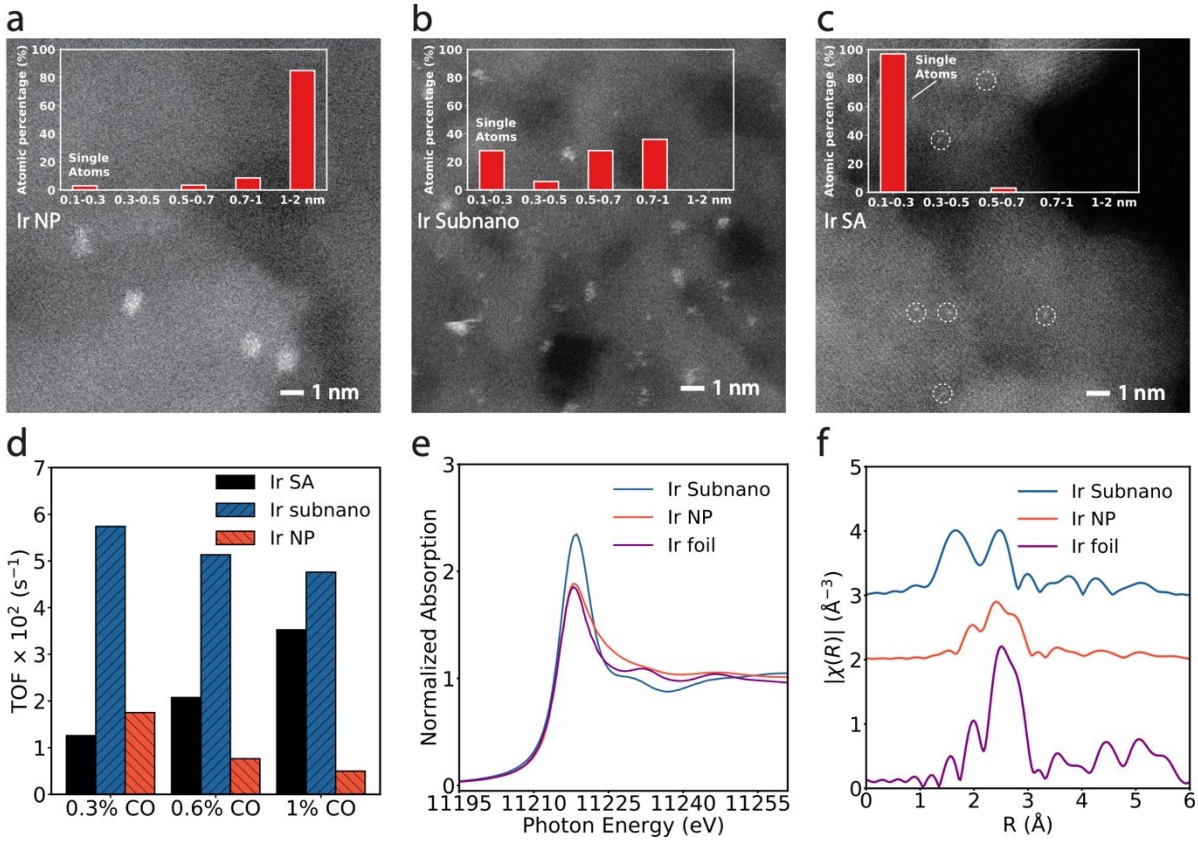

Fig. 1. Structural characterization and CO oxidation performance of $MgAl_2O_4$ supported Ir catalysts. HAADF-STEM images and histograms of (a) $Ir_{NP}/MgAl_2O_4$, (b) $Ir_{Subnano}/MgAl_2O_4$, and (c) $Ir_{SA}/MgAl_2O_4$. (d) Low-temperature CO oxidation performance of $Ir_{SA}/MgAl_2O_4$, $Ir_{Subnano}/MgAl_2O_4$ and $Ir_{NP}/MgAl_2O_4$ measured at 150 °C, at various P_{CO} (0.3 kPa, 0.6 kPa, 1 kPa) and P_{O2} at 10 kPa. (e) XANES and (f) EXAFS results of the Fourier transformed k^2-weighted χ(k) data measured on pretreated $Ir_{Subnano}/MgAl_2O_4$, pretreated $Ir_{NP}/MgAl_2O_4$ (1wt.%) and Ir foil. Δk = 2.6-12.5 $Å^{-1}$.

To provide more insights on the electronic properties and local coordination of Ir, we conducted XAS on the $Ir_{Subnano}/MgAl_2O_4$ (Fig. 1e, f). The magnitude of the Fourier transformed extended X-ray absorption fine structure (EXAFS) spectra (Fig. 1f) show peaks consistent with Ir–Ir and Ir–O scattering paths. Indeed, the EXAFS modeling results (Table S3) for $Ir_{Subnano}/MgAl_2O_4$ after reduction in H_2 show Ir–Ir and Ir–O coordination numbers of 3.5 ± 1.3 and 3.2 ± 0.5, respectively. The EXAFS results are consistent with the small subnanometer Ir clusters measured by HAADF-STEM (Supplementary

Information Figs S3–S6). The Ir–O coordination number for $Ir_{Subnano}/MgAl_2O_4$ is significantly higher than $Ir_{NP}/MgAl_2O_4$ (also in Supplementary Information, Table S3), which can be attributed to the contribution from the presence of Ir single atoms (~28%, Fig. 1a) and Ir atoms in the subnanometer clusters at the $MgAl_2O_4$ interface. Additionally, the high Ir–O coordination is consistent with the higher white line intensity observed in X-ray absorption near edge structure (XANES) region compared with that on Ir foil and Ir nanoparticles on $MgAl_2O_4$ (Fig. 1e). The results indicate that Ir in the subnanometer clusters in $Ir_{Subnano}/MgAl_2O_4$ is more electron deficient compared to 1–1.5 nm nanoparticles on the $MgAl_2O_4$ ($Ir_{NP}/MgAl_2O_4$). The activity of the supported metal catalysts is dependent on the metal oxidation state.[38] The oxidation state of the H_2 pretreated $Ir_{Subnano}/MgAl_2O_4$ was analyzed by the white-line intensity of the XANES spectra at Ir L_3-edge by comparing to Ir references. Supplementary Information Fig. S7 shows that the white-line intensity of $Ir_{Subnano}/MgAl_2O_4$ is between the Ir foil (Ir^0) and IrO_2 (Ir^{+4}). This shows that the average Ir oxidation of the $Ir_{Subnano}/MgAl_2O_4$ is between 0 and +4 and around +2. In comparison, the white-line intensity of $Ir_{NP}/MgAl_2O_4$ is only slightly higher than the Ir foil which suggests the Ir oxidation state is close to 0. The higher oxidation state of the $Ir_{Subnano}/MgAl_2O_4$ is attributed to the higher contribution of the metal-support interaction (formation of Ir–O bond at the interface) on smaller-sized clusters (0.6–0.8 nm), which can be seen by the Ir-O coordination from the EXAFS modeling results (Table S3). The oxidation state of the $Ir_{SA}/MgAl_2O_4$, was found to be higher than $Ir_{Subnano}/MgAl_2O_4$ and close to IrO_2 (i.e. oxidation state ~ +4, consistent with our previous DFT calculations)[39] due to the lack of Ir-Ir coordination and the higher coordination with oxygen from the support.

During low-temperature CO oxidation at 155 °C, the turnover frequency (TOF) on $Ir_{Subnano}/MgAl_2O_4$ at various CO partial pressures is up to 10 and 5 times higher than $Ir_{NP}/MgAl_2O_4$ and $Ir_{SA}/MgAl_2O_4$, respectively (Fig. 1d) where TOF is normalized with the surface Ir atoms measured by chemisorption for all three catalysts. The reaction orders in CO and O2 and the apparent activation energy (Table 1 and Supplementary Information Figs. S8–S10) provide insights on the CO oxidation mechanism and how it changes with Ir nuclearity in the three catalysts. For $Ir_{NP}/MgAl_2O_4$, the negative order (−1) in CO and positive order (+1) in O_2 indicate that the surface is poisoned by CO and O_2 activation is the rate limiting step as typically observed on supported platinum group metal nanoparticles.[40] On Ir single atoms, a facile O_2 activation, and an Eley–Rideal rate limiting step were reported in our previous work resulting in a zero order in O_2 and positive order (+1) in CO, respectively.[19] In contrast, the Ir subnanometer clusters (~0.7 nm, $Ir_{Subnano}/MgAl_2O_4$) show 0 order in CO and +0.4 order in O_2 (Supplementary Information Figs S8–S9). The results indicate a different reaction mechanism on Ir subnanometer clusters than that on single atoms or nanoparticles (1–1.5 nm). The CO oxidation activity is almost independent of CO partial pressure over a large CO partial pressure range (0 ± 0.2 order over a 50x increase in CO partial pressure, Supplementary Information Fig. S8a) suggesting that CO adsorption requires a different site than O_2 adsorption. In fact, the reaction orders are similar to those measured for Pt clusters supported on CeO_2[31, 41] and on TiO_2[42] where the reaction follows a two-site mechanism at the metal-support interfacial sites. Therefore, we hypothesize that the abundant metal-support interfacial sites on the Ir subnanometer clusters are likely involved in facilitating the O_2 adsorption and activation steps.

Table 1. Reaction orders and heats of adsorption (ΔH_{ads}) of CO and O_2 on $MgAl_2O_4$ supported Ir nanoparticles, subnanometer clusters and single atoms.

Catalyst	CO reaction order[a]	O_2 reaction order[b]	ΔH_{ads} of CO (kJ/mol)	ΔH_{ads} of O_2 (kJ/mol)
$Ir_{NP}/MgAl_2O_4$	−1 ± 0.1	+0.9 ± 0.1	-150	-330
$Ir_{Subnano}/MgAl_2O_4$	0 ± 0.02	+0.4 ± 0.03	-207 (-254)[c]	-515 (-529)[c]
$Ir_{SA}/MgAl_2O_4$	+0.9 ± 0.1	+0.1 ± 0.05	-230 ref. 19	-

[a] The CO reaction order was measured at P_{O_2}= 10 kPa and P_{CO} between 0.3-10 kPa (see Fig. S8).

[b] The O_2 reaction order was measured at P_{CO} = 1 kPa and P_{O_2} between 2-14 kPa (see Fig. S8).

[c] Heat of adsorption from DFT calculations on Ir_4 cluster supported on $MgAl_2O_4$ as shown in Fig. S11d (CO) and Fig. S12 (O_2).

The binding energies of CO and O_2 provide important insights on the reaction mechanism. CO microcalorimetry results (Table 1 and Supplementary Information Figs S13–15) show that subnanometer clusters adsorb CO strongly with an adsorption energy of 207 kJ/mol (average at low coverage, based on two measurements), which is much stronger than the binding of CO to Ir nanoparticles (150 kJ/mol at low CO coverage), and similar to the CO binding to Ir single atoms (230 kJ/mol from DFT calculations[19]). Similarly, the O_2 adsorption energy on the Ir subnanometer clusters is also much higher than that on nanoparticles 515 vs. 330 kJ/mol at low coverage. The strong O_2 adsorption on the Ir subnanometer clusters suggests that O_2 adsorption and activation could be more competitive than on Ir nanoparticles. However, competitive adsorption on the same Ir site should result in a CO order that changes with the CO partial pressure. Since the CO order was close to zero over 50x change in CO partial pressure (Supplementary Information Fig. S8a), the reaction orders are more consistent with O_2 adsorption and activation at the Ir-$MgAl_2O_4$ interfacial sites while the remaining sites are covered by strongly adsorbed CO (i.e. a two-site mechanism, which will be discussed further below).

To test the hypothesis of a two-site mechanism and provide more details on the reaction mechanism, we conducted *in-situ* diffuse reflectance infrared Fourier transform spectroscopy (DRIFTS) and EXAFS coupled with *in-situ* and *operando* high energy resolution fluorescence detected (HERFD)-XANES experiments. *In-situ* CO/O_2 cycling spectroscopic experiments were first performed at room temperature to probe the surface structure via CO/O_2 adsorptions and to depict an incomplete reaction cycle. *In-situ* HERFD–XANES and DRIFTS spectra on the CO saturated $Ir_{Subnano}/MgAl_2O_4$ (after reduction in H_2) are shown

in Fig. 2a, b (red spectra). When flowing O_2 on the CO covered $Ir_{Subnano}/MgAl_2O_4$ at room temperature, a significant increase in the white line intensity in HERFD–XANES was observed (Fig. 2a, blue) and the corresponding DRIFTS spectrum (Fig. 2b, blue) showed a blue shift where the ν_{CO} band shifted from 2033 to 2040 cm^{-1} indicating an increase in the oxidation state of Ir. In addition to the changes observed in HERFD–XANES and DRIFTS when flowing O_2, CO_2 was also detected in the on-line mass spectrometer (Supplementary Information Fig. S16), which indicates that O_2 could react with some of the adsorbed CO followed by co-adsorption with CO on the subnanometer Ir clusters at room temperature. In addition, surface carbonates at 1691 cm^{-1} in DRIFTS, were also detected during the room-temperature O_2 flow, which is another indication of CO_2 formation (Supplementary Information Fig. S17). Consistent with HERFD–XANES and DRIFTS, when the gas was switched from CO to O_2, the Ir–O coordination number from EXAFS increased from 3.2 to 4.1 indicating oxidation of the Ir subnanometer clusters (Fig. 2c, d and Supplementary Information, Table S3 and Fig. S18). When flowing CO again after the oxygen step, a decrease in the white line intensity was observed in HERFD–XANES (Fig. 2a, orange), but it was still higher than the white line of the initial spectrum in CO indicating that Ir does not return to the initial reduced state and that some adsorbed O* was still present. This can also be seen in DRIFTS after CO re-adsorption (yellow spectrum in Fig. 2b) where an extra shoulder at 2075 cm^{-1} was observed which is consistent with adsorbed CO on more oxidized Ir sites (i.e. CO* co-adsorbed with O* on Ir). It is important to note that CO was detected on Ir in DRIFTS under all conditions indicating that CO is strongly adsorbed on the reduced Ir subnanometer clusters which is consistent with the CO microcalorimetry results. More importantly, similar results were observed on another subnanometer $Ir/MgAl_2O_4$ catalyst prepared using $Ir_4(CO)_{12}$ (average size 0.5–0.6 nm, denoted as $Ir_{subnano\_Ir4}/MgAl_2O_4$, see Supplementary Information Figs. S19 and S20) indicating that the observed Ir behavior is due to the size being in the subnanometer regime and not necessarily specific to the synthesis or pretreatment conditions.

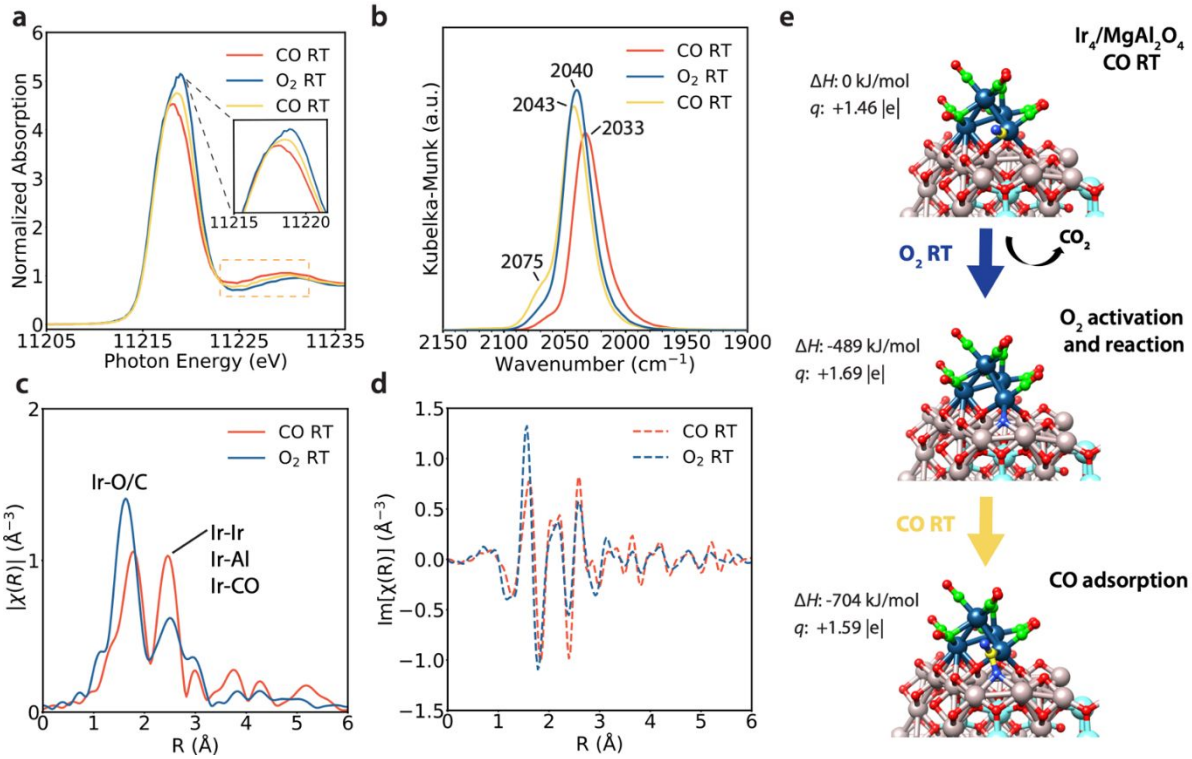

Fig. 2. Probing the surface structure of $Ir_{Subnano}/MgAl_2O_4$ under CO or O_2 atmosphere at room temperature. (a-d) HERFD–XANES, DRIFTS and EXAFS results of $Ir_{Subnano}/MgAl_2O_4$ under (a) HERFD–XANES spectra of subnanometer cluster sample A in flowing CO (1 kPa) at room temperature (red), in flowing O_2 (1 kPa) at room temperature (blue), and then in flowing CO (1 kPa) at room temperature (orange). (b) DRIFTS spectra in the ν_{CO} region characterizing the spectra of $Ir_{Subnano}/MgAl_2O_4$ when flowed CO (1 kPa) at room temperature (red), flowed O_2 (1 kPa) at room temperature (blue), and then flowed CO (1 kPa) at room temperature (orange). EXAFS magnitude (c) and imaginary (d) parts of the Fourier transformed k^2-weighted $\chi(k)$ data measured on the pretreated $Ir_{Subnano}/MgAl_2O_4$ when flowing CO and then O_2 at room temperature. Δk = 2.6–12.5 $Å^{-1}$. (e) Proposed states from DFT corresponding to the CO, O_2, and CO treatments. The relative energy (ΔH) and average Bader charge (q) of all four Ir are given. Al: gray; Mg: aqua blue; Ir: dark blue; O: royal blue for the oxygens involved in the reaction and red for other oxygens; C: yellow for the carbon involved in the reaction and green for other carbons.

The *in-situ* HERFD–XANES and DRIFTS results at room temperature are qualitatively similar to those we previously reported on single atom Ir supported on $MgAl_2O_4$[19] and strongly suggest that oxygen vacancies at the Ir-$MgAl_2O_4$ are involved in

the CO oxidation reaction mechanism. To provide more insight, we performed DFT calculations on Ir_4 clusters supported on the (111) O_2(Al) terminated $MgAl_2O_4$ surface as a representative model of the Ir subnanometer clusters in the $Ir_{Subnano}/MgAl_2O_4$ catalyst (see model and DFT calculation details in the Supplementary Information). To be consistent with the experimental conditions, the DFT model structure simulated the $Ir_4/MgAl_2O_4$ catalyst after H_2 reduction, and the optimized structure is shown in Fig. S21. Specifically, the initial state has an oxygen vacancy at the Ir-$MgAl_2O_4$ interface to model the vacancies generated during the $Ir_{Subnano}/MgAl_2O_4$ catalyst reduction at high temperature (700 °C). This can be explained by the presence of the Ir_4 cluster which lowers the average oxygen vacancy formation energy from 220 kJ/mol to 174 kJ/mol for nearby surface oxygens. Using this structure of $Ir_4/MgAl_2O_4$ after reduction, the DFT calculation results show an average adsorption energy of -254 kJ/mol for CO (Supplementary Information Fig. S11) and average initial adsorption energy of -529 kJ/mol for O_2 (Supplementary Information Fig. S12), which are very similar to the experimentally measured initial heats of adsorption of -207 and -515 kJ/mol for CO and O_2, respectively. The agreement of heats of adsorption between experiments and DFT calculations indicate that the Ir_4 clusters provide a reasonable model for the $Ir_{Subnano}/MgAl_2O_4$ catalyst and will be used to provide insights on the CO oxidation mechanism. Fig. 2e shows a CO saturated Ir_4 cluster that represents the starting state after reduction followed by CO adsorption in the *in-situ* experiments, including an oxygen vacancy at the Ir-$MgAl_2O_4$ interface as discussed above. Adsorption of O_2 is exothermic and O_2 gets activated between the vacancy and CO adsorbed on the closest Ir atom before they react to form CO_2 and fill the vacancy with a total reaction energy of -489 kJ/mol for adsorption and reaction (Fig. 3e). Similar behavior was reported theoretically using DFT calculations where the interfacial Pt–O sites of Pt_{10}/Al_2O_3 were predicted to adsorb O_2 strongly and activate O_2 more facilely than the non-interfacial Pt atoms.[43] The estimated barrier for CO_2 formation on the Ir_4 cluster is negligible, consistent with the CO_2 formation detected experimentally when the CO saturated catalyst was exposed to O_2 at room temperature (Supplementary Information Figs. S16–S17). This is expected due to the large exothermic reaction energy (-489 kJ/mol) for CO reacting with an O_2 that is readily activated upon adsorption. Lastly, re-adsorption of CO leaves the Ir_4 cluster saturated with CO similar to the initial structure, but with a filled oxygen vacancy at the interface. This oxygen reacts with CO adsorbed to a nearby Ir site, forming a CO_2 like structure that is bound strongly to the surface, similar to those reported by Thang et al.[44] on Pt_4/TiO_2 and Nie et al.[11] on Pt_1/CeO_2. This ends the room temperature reaction pathway as this structure requires ΔH of +137 kJ/mol to desorb also in line with results from Thang et. al. on Pt_4/TiO_2,[44] and consistent with our experiments where no further reaction was observed at room temperature. In agreement with the white line intensities from HERFD–XANES, the average DFT calculated Bader charges of the Ir_4 cluster at the same states measured experimentally show that Ir gets partially oxidized upon exposure to O_2 (from +1.46 e to +1.69 e) then it does not get fully reduced (compared to the initial CO saturated cluster) when CO is re-adsorbed (+1.59 e) due to the filling of the oxygen vacancy.

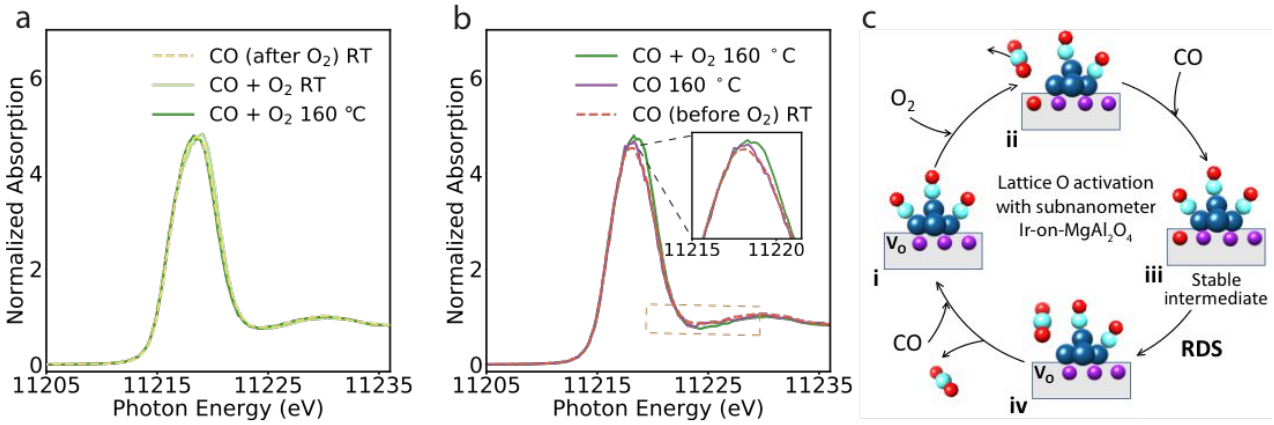

Fig. 3. Probing the surface structure of $Ir_{Subnano}/MgAl_2O_4$ under reaction condition. HERFD–XANES spectra of $Ir_{Subnano}/MgAl_2O_4$ (a) flowing CO (1 kPa) at room temperature after flowing O_2 (orange), then flowing CO (1 kPa) and O_2 (1 kPa) at room temperature, and then flowed CO (1 kPa) and O_2 (1 kPa) at 160 °C; (b) flow CO (1 kPa) only at 160 °C and in comparison with the CO+O_2 at 160 °C and the initial spectrum at room temperature in CO (after H_2 reduction). c) Proposed reaction cycle involving the lattice oxygen activation observed with $Ir_{Subnano}/MgAl_2O_4$ at 160 °C.

In order to complete the reaction cycle, the oxygen vacancy at the Ir-$MgAl_2O_4$ interface needs to be regenerated by reaction with CO which did not occur at room temperature as the *in-situ* DRIFTS and HERFD–XANES indicate. *In-situ/operando* HERFD–XANES experiments were performed at 160 °C (same temperature used for kinetics measurements in Fig. 1) to determine the state of Ir under reaction conditions. The Ir L_3 HERFD–XANES spectra were almost unchanged during CO and O_2 co-flow at both room temperature and reaction temperature of 160 °C (Fig. 3a), which indicates that the state of Ir under

reaction conditions is similar to the state where Ir is saturated with CO and the oxygen vacancies at the Ir-$MgAl_2O_4$ interface are filled (last structure in Fig. 2e). Furthermore, when the O_2 flow was stopped, a significant decrease in the white line intensity was observed and the HERFD–XANES spectrum was almost identical to the initial CO adsorption after H_2 reduction (Fig. 3b). The results indicate that exposure to CO at the reaction temperature can regenerate the vacancies at the Ir-$MgAl_2O_4$ interface which was not possible at room temperature (Fig. 2). Therefore, the results suggest that the rate limiting step involves a reaction between CO adsorbed on Ir and O* at the Ir-$MgAl_2O_4$ interface which was also proposed to be rate limiting for CO oxidation on Au/TiSBA-15.[45] Fig. 2e shows the final step containing a CO_2-like structure that is bound to the Ir_4 through the CO* and to the $MgAl_2O_4$ through the O*. This complex requires a high ΔH of +137 kJ/mol to desorb thus making it kinetically similar to a reaction between an absorbed CO*/Ir and O*/$MgAl_2O_4$ being rate limiting.

Fig. 3c shows a proposed reaction cycle and the accompanied structural changes observed on $Ir_{Subnano}/MgAl_2O_4$ involving lattice O activation at the Ir-$MgAl_2O_4$ interface. The interfacial lattice O vacancy (i) is filled by O_2 adsorption and reaction with adsorbed CO on Ir to form CO_2 (ii). CO then adsorbs on (ii) and the resulting structure with a filled O vacancy (iii) is the most stable intermediate in CO+O_2 at both room temperature and 160 °C. The rate determining step involves the reaction between adsorbed CO and the interfacial lattice O in (iii) to regenerate the O vacancy (iv), which was observed when flowing CO in the absence of O_2 at 160 °C. The cycle is then complete by adsorption of CO on (iv). The steps for this two-site mechanism are written as elementary steps in scheme 1. In this scheme, the rate determining step (RDS), step (4), is the reaction of a CO adsorbed on the Ir cluster with an O filled vacancy. We can eliminate the other steps as being rate determining as the reaction orders would be +1 in CO for step (1) being rate determining and +1 in O_2 for step (2) or (3) being rate determining. The DRIFTS and HERFD-XANES spectroscopy results in Figs. 2 and 3 indicate that the iridium clusters are covered in CO under reaction conditions due to the strong Ir-CO binding (see Table 1). The high CO coverage observed experimentally on Ir justifies the approximation of setting the coverage equal to 1 in the model. Additionally, since the reaction of CO on Ir with O_2 adsorbed on a vacancy at the Ir-support interface is facile (Fig. 2), the O_2* coverage can be neglected, making the O* the most abundant surface intermediate (MASI) for the support sites. These all combine to give the rate equation presented in scheme 1 (derivation in the SI) which is consistent with the 0 order in CO and the partial positive order in O_2 measured experimentally and also consistent with the in-situ/operando spectroscopy results in Figs. 2 and 3.

Fig. 4 shows a scheme summarizing the proposed CO oxidation reaction mechanism on $MgAl_2O_4$ supported subnanometer clusters in comparison to previously reported mechanisms on Ir single atoms and nanoparticles. On $Ir_{SA}/MgAl_2O_4$, a previous study by our group showed that CO binds very strongly to Ir_1 (-230 kJ/mol) and forms an Ir(CO) active complex that promotes the O_2 activation at the Ir-$MgAl_2O_4$ interfacial site. A second gas phase CO molecule then reacts with an interfacial surface O* via an Eley–Rideal mechanism. In this work, our results strongly suggest that a similar interfacial O_2 activation is involved on $MgAl_2O_4$ supported subnanometer Ir clusters. Different from the Eley–Rideal mechanism observed on $Ir_{SA}/MgAl_2O_4$, the reaction proceeds via a dual-site mechanism at the Ir-$MgAl_2O_4$ interface where CO from the Ir cluster reacts with O* from the support. For the rate determining step on SA and subnanometer clusters, the preference for an adsorbed CO to react with the interfacial O* as opposed to have a gas phase CO molecule on Ir_{SA} can be due to the availability of multiple CO molecules near the interface on the clusters (unlike one CO molecule for Ir_1). In contrast, the number of interfacial sites is limited on larger nanoparticles and CO oxidation is dominated by the reaction on the Ir metal sites via a Langmuir–Hinshelwood reaction mechanism where O_2 activation proceeds on a vacant site assisted by CO adsorbed on a neighboring site. Therefore, despite the stronger CO adsorption on Ir subnanometer clusters, the support provides CO-free sites at the Ir-$MgAl_2O_4$ interface where O_2 activation can proceed while on nanoparticles all neighboring Ir sites are poisoned by CO. We note that our results demonstrate that he activity of Ir subnanometer clusters is mostly contributed by the metal-support interfacial sites and the non-interfacial sites are almost inactive. Therefore, a correction could be made for the TOF results shown Fig. 1d to normalize the TOF of Ir subnanometer clusters with the interfacial Ir sites instead of all the surface Ir sites. At 0.3 kPa CO and 10 kPa O_2, the estimated TOF normalized to the interfacial sites of 0.77 nm subnanometer clusters is 6.2 and 8.6 times of the TOF of Ir NP and Ir SA, respectively (see Supplementary Information Table S5 for more details).

Scheme 1. Elementary Steps, site balances, and kinetic equations for the proposed reaction mechanism.

	Elementary Step	
(1)	$CO_{(g)} + Ir^* \leftrightarrow Ir(CO)^*$	
(2)	$O_{2(g)} + * \leftrightarrow O_2^{\#}$	
(3)	$Ir(CO)^* + O_2^{\#} \rightarrow CO_{2(g)} + Ir^* + O^{\#}$	
(4)	$Ir(CO)^* + O^{\#} \rightarrow CO_{2(g)} + Ir^* + \#$	RDS
	Site Balances	
Iridium	$[Ir(CO)^*] = 1$	
Support	$[O^{\#}] + [\#] = 1$	
	Kinetic Equation	
	$r_{CO_2} = \frac{2k_2k_3k_4P_{O_2}}{k_4(k_{-2} + k_3) + k_2k_3k_4P_{O_2}}$	

Note: Step (1) is exercised twice per mechanism cycle. The site balances have already included the assumptions that Ir is fully covered by CO and that O_2* coverage is negligible as discussed in the text.

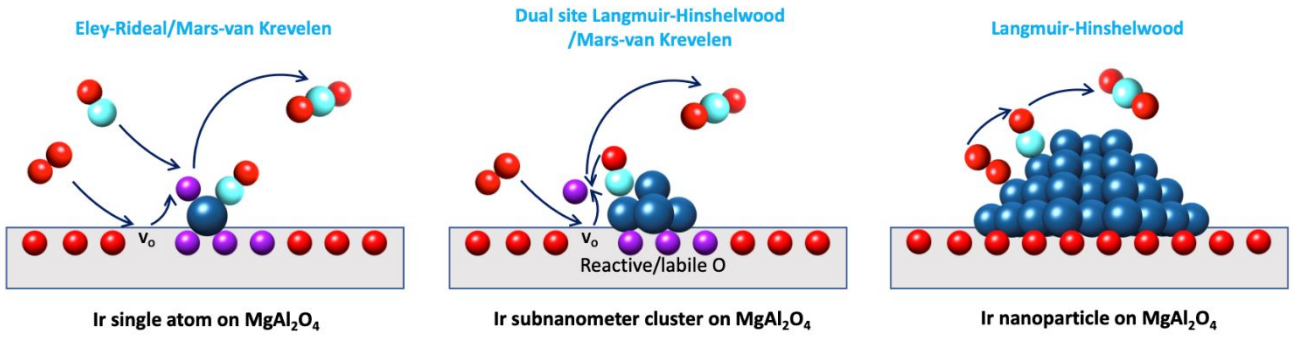

Fig. 4. Proposed reaction mechanisms of CO oxidation on $MgAl_2O_4$ supported single atoms, subnanometer clusters and nanoparticles. CO molecules that saturate the Ir subnanometer cluster and nanoparticle are not shown for simplicity.

To put our results in perspective, we will first discuss CO oxidation on metal clusters and nanoparticles supported on reducible oxides. On reducible oxides, the interfacial sites between the metal and the support play an important role in CO oxidation by providing sites for O_2 adsorption and activation. For Pt/CeO_2[31, 41, 46] and Pt/TiO_2[47], the lattice oxygen activation is facile and the reaction is dominated by the metal-support interfacial sites. For example, by varying the Pt size between 1.6–3 nm for Pt/CeO_2, Cargnello et al. showed that the low-temperature CO oxidation reactivity scales with the number of interfacial sites.[48] Similarly for Pt/TiO_2, the TOF based on interfacial Pt atoms is independent of Pt particle size between 1–10 nm.[47] On the other hand, in the subnanometer regime (<1 nm), significant promotion of O_2 activation at the Rh-TiO_2 interface was reported, where 0.4-0.8 nm Rh clusters showed better CO oxidation performance than the single atoms and nanoparticles.[24]

The reports on reducible metal oxide supports further show the significance of our work on $MgAl_2O_4$. Traditionally, $MgAl_2O_4$ is considered a non-reducible support and CO oxidation proceeds only on the metal sites of the supported nanoparticles. Our results are consistent with this definition when $MgAl_2O_4$ is used to support Ir metal nanoparticles (> 1nm). However, we show that by decreasing the Ir size in the subnanometer regime, the strong interaction between $MgAl_2O_4$ and Ir single atoms and subnanometer clusters activates the interfacial lattice oxygens similar to a reducible oxide. More importantly, the activation of interfacial lattice oxygens provides new, more efficient CO oxidation pathway compared to nanoparticles where the rate is limited by O_2 activation on a CO poisoned surface. Additionally, despite the similarity in lattice oxygen being involved in CO oxidation on Ir single atoms and subnanometer clusters, we show that the metal nuclearity has a strong effect on the mechanism and activity. Specifically, increasing the metal nuclearity from single atoms to subnanometer clusters resulted in the mechanism changing from Eley–Rideal/Mars–van Krevelen to a dual-site Langmuir–Hinshelwood/Mars–van Krevelen mechanism. Notably, the change in mechanism from single atoms, to subnanometer clusters, to nanoparticles, leads to a volcano-type dependence with the Ir subnanometer clusters being the most active. Furthermore, due to the different mechanism in the subnanometer regime, the initial CO binding energy fails to predict the activity of the catalysts. Therefore, our work shows that the change in mechanism in the subnanometer regime on metal supported catalysts provides opportunities to escape traditional reactivity descriptors and design more active metal catalysts.

Conclusions

Our work demonstrates that on a traditionally non-reducible oxide, decreasing the size of the metal into the subnanometer regime results in the emergence of properties similar to reducible oxides. Using advanced *in-situ/operando* characterization complemented by DFT calculations we show that the Ir–O interfacial sites of $MgAl_2O_4$ supported Ir subnanometer clusters (0.6–0.8 nm) participate in efficient CO oxidation and O_2 activation leading to enhanced activity compared with Ir nanoparticles (1–1.5 nm). Furthermore, detailed kinetic measurements reveal that the reaction mechanism for CO oxidation in the subnanometer regime is intrinsically different from that on nanoparticles and is strongly dependent on the metal nuclearity. While Ir single atoms are more active than nanoparticles due to their ability to activate interfacial O*, increasing the metal nuclearity in the subnanometer regime resulted in a change in the mechanism from Eley–Rideal to a dual-site Langmuir–Hinshelwood mechanism and enhanced activity. We show that the change in the reaction mechanism as a function of Ir nuclearity leads to a volcano-type dependence of the CO oxidation reactivity on $MgAl_2O_4$, a traditionally non-reducible oxide.

Experimental section

Synthesis and pretreatment

Two subnanometer clusters catalysts were prepared using different precursors. The first Ir/MgA_2O_4 subnanometer clusters catalyst (0.05 wt%, denoted as $Ir_{Subnano}/MgAl_2O_4$) was prepared

by wet impregnation using Ir nitrate. The $MgAl_2O_4$ support (Puralox MG 30, Sasol) was calcined at 500 °C for 4 hr before impregnation. 200 mL DI water was added to a Pyrex bottle and the pH was adjusted with nitric acid to 2.8. Proper amount of the Ir nitrate precursor (8.7 wt. % Ir, Furuya Metal CO. Ltd.) was added into the pH adjusted solution. 5 g of the $MgAl_2O_4$ support was then added into the solution while stirring for 2 hr. The final pH of the solution was 9.5. The solution was filtered out, and the solid sample was dried in air for 24 hr at room temperature. The sample was then dried at 80 °C (0.5 °C/min) for 4 hr and 100 °C (0.5 °C/min) for 4 hr before calcination at 500 °C for 4 hr with a ramp rate of 5 °C/min. The Ir in the solution after filtration was measured by inductively coupled plasma atomic emission spectroscopy and no Ir was detected. The sample was pretreated in 20 kPa H_2 in situ (80 sccm total) at 700 °C for 2 hr and cooled down to room temperature in the same gas. The second Ir/MgA_2O_4 subnanometer clusters catalyst (0.1 wt.%, denoted as $Ir_{Subnano\_Ir4}/MgAl_2O_4$) was prepared by wet impregnation using $Ir_4(CO)_{12}$. Proper amount $Ir_4(CO)_{12}$ (Sigma Aldrich) precursor was dissolved in 16 mL of toluene (Sigma Aldrich) in a 20 ml vial while flowing N_2 at room temperature. Then the dissolved $Ir_4(CO)_{12}$ toluene solution was injected into another vial containing 5 g $MgAl_2O_4$ (Puralox MG 28, Sasol) under N_2 flow. The sample was then dried under N_2 flow at room temperature overnight to evaporate the toluene. No calcination was performed on this catalyst. The CO and acac ligands were removed in-situ by treatment in He at 400 °C (10 °C/min) and then H_2 at 200 °C which led to the formation of subnanometer clusters as detailed below. The 2% Ir/ γ-Al_2O_3 (Ir nanoparticle sample, NP, average size 5–12 nm, denoted as Ir_{NP}/γ-Al_2O_3) was synthesized by incipient wetness impregnation. Ir nitrate (8.7 wt. % Ir, Furuya Metal CO. Ltd.) in aqueous solution was used as precursor and was diluted to achieve a final Ir weight loading of 2%. The Al_2O_3 support (Puralox TH 100/150, Sasol) was calcined at 550 °C for 4 hr before impregnation. After impregnation at room temperate for 24 hr, the 2% Ir/ γ-Al_2O_3 sample was dried at 80 °C for 12 hr with a slow ramp rate of 0.5 °C/min followed by heating to 100 °C (at 0.5°C/min) and dwelling for 4 hr. The dried sample was then calcined at 500 °C in air for 4 hr (5 °C/min). The preparation of the $Ir_{SA}/MgAl_2O_4$ and $Ir_{NP}/MgAl_2O_4$ were reported in our previous work.[19]

High energy resolution fluorescence detected-X-ray absorption near energy spectroscopy (HERFD–XANES)

HERFD–XANES measurements were collected at beamline 6-2 at the Stanford Synchrotron Radiation Light Source (SSRL). A liquid-nitrogen-cooled double-crystal Si(311) monochromator was equipped to select the energy of the incident beam with a flux of 3 x 10^{12} photons × s^{-1}. A Rowland circle spectrometer (radius 1 m) equipped with three spherically bent Si (800) analyzers and a silicon drift detector was used to select the Ir L_α (9175 eV) emission line with a measured resolution of 1.3 eV. An iridium foil was scanned in the transmission mode for initial energy calibration.

Each sample (120 mg in mass, 25–90 microns) was loaded into a packed bed flow reactor. The catalysts were characterized by *in-situ* XAS at the Ir L_3-edge (11215 eV) using an in-house built cell[49] with a 4 mm ID glassy carbon tube connected to the gas line using graphite ferrules and heated by a stainless-steel heating block equipped with four 100 W heating cartridges (Watlow). The in-situ reactor assembly was protected from oxidation by an air-free box with polyimide film X-rays windows and continuous He or N_2 flow. Two type-K thermocouples were used to monitor and control the heating block and the catalytic bed temperature. A portable gas delivery system equipped with 5 MFCs (Brooks - SLA5800) was used to control the gas flow. The composition of effluent gases was measured by an online quadrupole mass spectrometer (Hiden HPR20). Samples were pretreated the same as the previous section.

All HERFD–XANES spectra were measured within 2 min and three to six scans were averaged to improve signal-to-noise ratio. The analysis of the HERFD–XANES data was carried out with the software ATHENA of the Demeter package [50, 51]. The edge, determined by the first inflection point of the absorption edge of the Ir foil, was calibrated to the reported Ir L_3 energy, 11215 eV. This calibration was used to calibrate a known glitch in the monochromator observed in the I_0 signal of each scan. A least-squares Gaussian fit of the glitch, determined the error in the energy calibration of the samples to be 0.022 eV. Energy calibration was achieved by aligning the glitch in each scan to the glitch in the Ir foil reference scans. Three to six scans per sample were averaged with the averaged spectra being used for deglitching and normalization. The averaged spectrum was processed by fitting a second-order polynomial to the pre-edge region and subtracting this from the entire spectrum. Edge energy was determined by the first derivative of the normalized absorbance. The data were normalized by dividing the absorption intensity by the height of the absorption edge.

Extended X-ray absorption fine structure (EXAFS)

In-situ XAS measurements at Ir L_3 (11215.0 eV) edge was performed at the Stanford Synchrotron Radiation Light Source (SSRL) beamline 9-3 in fluorescence mode at the Ir L_3-edge (11215.0 eV) using an in-house built cell with a 4 mm ID glassy carbon tube[16,17] Beam line 9-3 is a 16-pole, 2-Tesla wiggler side station with vertically collimating mirror for harmonic rejection and a cylindrically bent mirror for focusing. The photon energy was selected using a liquid-nitrogen-cooled, double-crystal Si (220) ϕ = 90° monochromator. Samples were scanned simultaneously in transmission and fluorescence detection modes using ion chambers (I_0 filled with N_2 and I_t and I_{ref} filled with Ar) and a 100-element solid-state Ge monolith detector (Canberra), respectively. An Ir standard (Ir black powder) was scanned simultaneously with each sample for energy calibration. Step-scanning X-ray absorption spectra were measured from up to photoelectron wave number k of 14 $Å^{-1}$. The catalysts were pretreated similar to before the catalytic measurements, then cooled to room temperature in pure H_2 flow (50 sccm) and the extended x-ray absorption fine structure (EXAFS) spectra were collected at room temperature under pure H_2 flow. XANES and EXAFS data processing and analysis were performed using Athena and Artemis programs of the

Demeter data analysis package[18,19]. Multiple scans were collected and merged after alignment, thirty scans for at 10-ID and nine scans at 9-3. $\chi(k)$ was obtained by subtracting smooth atomic background from the normalized absorption coefficient using the AUTOBK code. The theoretical EXAFS signal was constructed using the FEFF6 code[20] and fitted to the data in *R*-space using the Artemis program. For modeling the Ir–Ir scattering, an fcc crystal structure with a lattice constant of 3.92 Å was used. The Ir–Al/Mg, Ir–O, Ir–C, Ir–$O_{(CO)}$ scattering paths were simulated from density functional theory calculated structure of CO adsorbed on Ir on the (211) step site[9]. The theoretical EXAFS scattering paths were fit to the data in *R*-space using the Artemis program of the Demeter package. The spectra were fit by varying the coordination number of the single scattering Ir–O, Ir–C, Ir–$O_{(CO)}$, Ir–Ir and Ir–Al/Mg paths, the bond length disorder (σ^2), and the effective scattering lengths for each path and the correction to the threshold energy, ΔE_0 (except for Ir–Ir, ΔE_0 was the same for all scattering paths since they are calculated from one FEFF calculation on the same structure). The double (O–C–Ir, degeneracy = 2) and triple (C–O–C–Ir, degeneracy = 1) scattering paths of Ir–C–O were included in the model using the same scattering length and σ^2 as Ir–$O_{(CO)}$ and therefore did not add any extra parameters to the model. S_0^2 (the passive electron reduction factor) was obtained by first analyzing the spectrum for an Ir black, and the best fit value (0.83) was fixed during the fitting. The *k*-range used for Fourier-transform of the $\chi(k)$ was 2.6–12.5 $Å^{-1}$ and the *R*-range for fitting was 1.1–2.9 Å. The best parameters fit using *k*-weight of 1,2,3 are reported. We note that the spectra under the different conditions were fit simultaneously with shared common parameters (i.e. ΔE_0 for the same paths) to minimize the fit uncertainty.

Diffuse-reflectance infrared Fourier-transform spectroscopy

DRIFTS was used to characterize the interaction of the supported Ir catalysts with CO. The *in-situ* DRIFTS experiments were performed using a Thermo Scientific IS-50R FT-IR equipped with an MCT/A detector. A spectral resolution of 4 cm^{-1} was used to collect spectra, which are reported in the Kubelka-Munk (KM) units. Approximately 50 mg sample (25-90 μm diameter particles) was loaded in the Harrick Praying Mantis high-temperature DRIFTS reaction chamber. The chamber was sealed and connected to a flow system with temperature control, and gases were flown through the sample at atmospheric pressure. Each reported spectrum is an average of 32 scans. The supported Ir samples were pretreated *in-situ* in the DRITS cell before collecting the spectra. The gas pretreatment procedure was the same as mentioned above. A spectrum under N_2 after the pretreatment was collected as the background for each catalyst.

Microcalorimetry

Microcalorimetry was performed on a Setaram SENSYS Evo DSC calorimeter with a self-built U-shape sample tube. The U-shape sample tube was connected to a Micromeritics 3Flex for the adsorption quantity measurement and temperature control. 70 mg catalyst was put in the U-shape reactor each time. The gas pretreatment procedure was the same as mentioned above. After pretreatment, the samples were exposed to ultra-high vacuum (UHV) with pressure below 10^{-5} mmHg. For the first set of doses, adsorption heat of both chemisorption and physisorption CO/O_2 was measured. The CO/O_2 adsorption experiments were measured at 30 °C with pressure between 0-300 mm Hg for O_2 calorimetry and 0–20 mmHg for CO calorimetry.

Scanning transmission electron microscopy

Aberration-corrected electron microscopy images for $Ir/MgAl_2O_4$ samples were taken on FEI TITAN 80-300 in STEM mode using a high angle annular dark field (HAADF) detector. The resolution is 0.1 nm, with the CEOS GmbH double-hexapole aberration corrector. To calculate the atomic percentage from multiple STEM images, the number of atoms per particle (*N*) was estimated with a hemispherical model [18, 52]:

$$N = \frac{\pi D^3 \rho N_A}{6 M_w} \quad (1)$$

where *D* is the nanoparticle diameter, ρ is the bulk metal density, N_A is Avogadro's number, and Mw is the metal molecular weight.

X-ray diffraction

X-ray diffraction (XRD) was performed on fine powdered samples of the indicated pre-treatment. XRD was performed on a Bruker D2 PHASER operating at 30 kV and 10 mA. The radiation source was a Cu filament at the Kα edge (λ = 1.54184 A). The samples were measured from 20° to 80° (2*θ) with a step size of 0.1° with a sample time of 1 s.

CO oxidation kinetic measurements

CO oxidation kinetic measurements were performed under differential conditions (<3% conversion) in a conventional laboratory tubular plug flow reactor (7 mm ID quartz tube). Dilution experiments were performed according to Koros-Nowak test to determine the necessary dilution ratio for measurements under strict kinetic control without mass and heat transfer effects[53-55]. The catalysts (after intraparticle dilution) were pressed and sieved into a 106–250 μm diameter fraction. The dilution ratio test to eliminate transport limitations was performed on $Ir_{NP}/MgAl_2O_4$ (1wt.%) using SiO_2 (Silica gel, for chromatography, 0.075–0.250 mm particle size and 150 Å pore size) calcined at 850 °C as the diluent. Intraparticle dilutions ratio of 1:40, 1:200 and 1:1000 showed no difference in activity under different CO and O_2 conditions between 145 °C and 170 °C, which indicates the measured catalytic activity were evaluated under kinetic control without transport artifacts. Based on the dilution test, the $Ir_{NP}/MgAl_2O_4$ (0.2 wt.%) was diluted with silica at a 1:20 ratio, and the $Ir_{SA+NP}/MgAl_2O_4$ (1 wt.%) and $Ir_{NP}/MgAl_2O_4$ (1wt.%) were diluted with silica at a 1:40 ratio, and the $Ir_{SA}/MgAl_2O_4$ and the $Ir_{Subnano}/MgAl_2O_4$ required no dilution because of the low Ir loading. 0.2–0.6 g of each catalyst (including dilution) was

loaded in the reactor to keep the conversion below 3% under all conditions measured. The total flow rate during the measurements was between 75–100 sccm. Negligible activity (~1/10 activity of the lowest loading catalyst, 0.0025 wt.%, sample 4) was measured on the $MgAl_2O_4$ support compared to all the catalysts. Each catalyst pretreatment was the same as mentioned above, and the total flow rate during pretreatment was kept at 80 sccm. The catalyst temperature was measured by a K-type thermocouple (OMEGA) attached at the center of the catalyst bed on the outside of the tube. After pretreatment, CO (5%, balance N_2, certified grade Airgas) was mixed with pure O_2 (99.999% Airgas) and He (99.999% Airgas, equipped with moisture/O_2 trap, Agilent OT3-2) at 35 °C to control the partial pressures of CO and O_2 (by varying their flowrates using Brooks mass flow controllers SLA5800 series). The CO gas line was equipped with a metal carbonyl purifier (Matheson, NanoChem Metal-X) to remove the trace amount of metal carbonyl and a molecular sieve 3A (8–12 mesh) trap to remove trace (ppm) levels of CO_2. No CO_2 (above baseline level in He) was detected in the mass spectrometer with the CO or O_2 flowing during a blank test. The reactor was heated from room temperature to the reaction temperature at 3 °C/min in 0.5 kPa CO and 10 kPa O_2 balanced with He. During the steady state kinetic measurements, the conversion of CO was always below 3% by varying the total flow rate between 75–100 sccm. To investigate the effect of CO partial pressure on reaction rate, the partial pressure of O_2 was held constant at 10 (or 2) kPa and the partial pressure of CO was varied between 0.2–1.0 kPa. To investigate the effect of O_2 partial pressure, the CO partial pressure was held constant at 0.2 kPa and the partial pressure of O_2 was varied between 2–14 kPa. To investigate the effect of temperature and measure the apparent activation energy, the CO and O_2 partial pressures were kept at 1 kPa and 10 kPa, respectively. The temperature was varied between 145-160 °C. The kinetic experiments were reproduced using two different aliquots from the same batch and also reproduced using two different batches of catalyst. We note that we rigorously monitored the catalyst stability by re-measuring the catalyst activity periodically throughout the experiment under the first condition measured. The activity was stable (< 10% deactivation) for each catalyst tested during the entire kinetic measurement. The composition of the effluent gases was measured by a gas chromatograph (Inficon Micro GC Fusion with two modules each with a separate carrier gas, injector, column and thermal conductivity detector (TCD). Column A: Rt-Molsieve 5A, 0.25 mm ID (10m) using Ar as carrier gas. Column B: Rt-Q-Bond 0.25 mm ID (12m) using He as carrier gas.

Calculation of Ir dispersion and turnover frequency (TOF)

Ir dispersion is defined as the ratio of surface Ir sites to total Ir atoms in the catalyst. Ir dispersion could be calculated by the following equation: $\text{Ir Dispersion} = \frac{\text{Surface Ir sites (mol)}}{\text{Total Ir sites (mol)}}$. Dispersion of Ir in the $Ir_{SA}/MgAl_2O_4$, $Ir_{Subnano}/MgAl_2O_4$ and $Ir_{NP}/MgAl_2O_4$ catalysts was calculated based on the volumetric CO chemisorption measurements and the Ir loading. To convert the measured CO uptake from chemisorption to Ir sites, we used CO: Ir ratio. The CO: Ir for $Ir_{SA}/MgAl_2O_4$ is 2:1 based on the dicarbonyl ($Ir(CO)_2$) configuration. The CO: Ir for $Ir_{Subnano}/MgAl_2O_4$ or $Ir_{NP}/MgAl_2O_4$ is both assumed as 1:1 based on the adsorption configuration. Based on the volumetric CO adsorption results (Table S4) and the above CO to Ir ratios, the dispersion of the $Ir_{SA}/MgAl_2O_4$, $Ir_{Subnano}/MgAl_2O_4$ and $Ir_{NP}/MgAl_2O_4$ catalysts is 100%, 90% and 90%.

TOF is defined as the number of molecules reacted at each available surface site per unit time.

$\text{TOF } (s^{-1}) = \frac{\text{Reactoin rate per g catalyst } (mol.s^{-1}.g^{-1})}{\text{Molar concentration of surface Ir per g catalyst } (mol.g^{-1})}$. Molar concentration of surface Ir per g catalyst ($mol.g^{-1}$) is obtained from on the volumetric CO adsorption measurement by measuring the molar of CO per g catalyst and using the CO: surface Ir ratio. Molar concentration of surface Ir per g catalyst $(mol.g^{-1}) = \frac{\text{CO adsorbed per g of catalyst } (mol.g^{-1})}{\text{CO:surface Ir}}$.

Density Functional Theory

DFT calculations were performed using the CP2K computational code[56-61]. The generalized gradient approximation parameterized by the spin-polarized Perdew-Burke-Ernzerhof (PBE) functional was used to treat the exchange-correlation potential[62-66]. All elements used the double ζ valence polarized Gaussian basis sets with an auxiliary plane-wave basis set with a cutoff energy of 480 Ry with Goedecker-Teter-Hutter potentials used for the core electrons[67, 68]. The calculations consist of only gamma point sampling. The DFT-D3 van der Waals correction was applied[69]. In geometry optimizations[70], the forces were converged to $4.5x10^{-4}$ Hartree/Bohr. Bader charge analysis was calculated using the Bader Charge Analysis code from the Henkelman group[71-74]. Enthalpies were approximated as the DFT energetics reported in CP2K. In order to compensate for the known O_2 over binding from PBE functional, the gas phrase energy of O_2 was increased by 0.75 eV[19].

Optimized spinel bulk calculations and surface calculations were taken from previous work[19, 75] and were used to determine lattice constants and surface terminations respectively. Those previous results showed that the (111) O_2(Al) terminated spinel surface was the most stable under a wide variety of conditions and was thus chosen. The slabs (Fig s1a) were composed of 2 unit cells in the two surface lattice directions and 3 unit cells in the dimension perpendicular to the surface. The bottom two layers of the slab were then fixed to reduce computational time and simulate bulk behavior. 15 Å of vacuum separated the slabs, as this is a periodic calculation.

Different geometries of four iridium atom clusters were placed on the (111) spinel surface, including the square planar geometry.[76] The most energetically favorable was the near tetrahedral configuration with three iridium atoms bound to the surface.[77, 78] Fig. S21a was chosen to be our representative Ir_4 cluster. With a representative Ir_4 cluster established, we began investigating the effects this would have on the surface termination, specifically number of surface oxygens. The addition of the Ir_4 cluster lead to a decrease in the average oxygen vacancy formation energy from 220 to 174 kJ/mol for the O* around the cluster. We define around the Ir_4 cluster as all surface O since the periodic unit cell ensures the O can never be more than 4.701 angstroms from an Ir atom. In order to

investigate the proper surface termination to use, we calculated the surface vacancy formation energy of each O and removed a single O at a time until all surface O had a vacancy formation energy of 1 eV or more. This was done to simulate the reducing environment the catalyst was exposed to. The O's removed are those highlighted in Fig. S21b.

To calculate the initial binding energies of O_2 on Ir_4, different combinations of 2 O species were added individually to the iridium cluster (Fig. S20). We calculated the dissociative binding energy to be -529 kJ/mol O_2. This compares favorably to the -480 to -550 kJ/mol observed from experiments for the initial binding energy of oxygen. Similarly, CO was added to the cluster in various amounts (1–4 molecules at a time) until saturated to represent a CO covered cluster (Fig. S4). The average binding energy for CO was -254 kJ/mol. The resulting CO covered structure is similar in structure to a distorted $Ir_4(CO)_{12}$ organometallic species[79] but with three CO molecules replaced with surface bonds (Fig. S19).

With the CO covered Ir_4 cluster established as our model after reduction and CO dosing, we probed the surface oxygen vacancies again to see if any oxygens would be removed after the addition of the CO. All Os were found to have a vacancy formation energy of at least 1 eV, the cut-off we considered. The average surface vacancy formation energy for the oxygen species increased from 339 kJ/mol to 419 kJ/mol from the addition of the COs.

Conflicts of interest

There are no conflicts to declare.

Acknowledgements

This research was primarily sponsored by the Army Research Office and was accomplished under Grant Numbers W911NF-16-1-0400 and W911NF-19-1-0308. The views and conclusions contained in this document are those of the authors and should not be interpreted as representing the official policies, either expressed or implied, of the Army Research Office or the U.S. Government. The U.S. Government is authorized to reproduce and distribute reprints for Government purposes notwithstanding any copyright notation herein. Use of the Stanford Synchrotron Radiation Light Source (SSRL, beamline 9-3, user proposal 4645), SLAC National Accelerator Laboratory is supported by the U.S. Department of Energy, office of Basic Energy Sciences under Contract No. DE-AC02-76SF00515. Additional support by the Consortium for Operando and Advanced Catalyst Characterization via Electronic Spectroscopy and Structure (Co-ACCESS) at SLAC is acknowledged. Co-ACCESS, is supported by the U.S. Department of Energy, Office of Science, Office of Basic Energy Sciences, Chemical Sciences, Geosciences and Biosciences under Contract DE-AC02-76SF00515. STEM imaging was performed at the William R. Wiley Environmental Molecular Science Laboratory (EMSL) sponsored by the U.S. Department of Energy, office of Biological and Environmental Research located at Pacific Northwest National Laboratory (PNNL) under science theme proposal 49326. The computational resource used in this work is provided by the advanced research computing at Virginia Polytechnic Institute and State University.

References

1. S. Ji, Y. Chen, X. Wang, Z. Zhang, D. Wang and Y. Li, *Chem. Rev.*, 2020, **120**, 11900-11955.
2. S. Mitchell, E. Vorobyeva and J. Perez-Ramirez, *Angew. Chem. Int. Ed.*, 2018, **57**, 15316-15329.
3. L. C. Liu and A. Corma, *Chem. Rev.*, 2018, **118**, 4981-5079.
4. S. K. Kaiser, Z. Chen, D. Faust Akl, S. Mitchell and J. Pérez-Ramírez, *Chem. Rev.*, 2020, **120**, 11703-11809.
5. S. P. Ding, M. J. Hulsey, J. Perez-Ramirez and N. Yang, *Joule*, 2019, **3**, 2897-2929.
6. A. Q. Wang, J. Li and T. Zhang, *Nat. Rev. Chem.*, 2018, **2**, 65-81.
7. L. C. Liu, U. Diaz, R. Arenal, G. Agostini, P. Concepcion and A. Corma, *Nat. Mater.*, 2017, **16**, 132-138.
8. J. Fu, J. Lym, W. Zheng, K. Alexopoulos, A. V. Mironenko, N. Li, J. A. Boscoboinik, D. Su, R. T. Weber and D. G. Vlachos, *Nat. Catal.*, 2020, **3**, 446-453.
9. S. Vajda, M. J. Pellin, J. P. Greeley, C. L. Marshall, L. A. Curtiss, G. A. Ballentine, J. W. Elam, S. Catillon-Mucherie, P. C. Redfern, F. Mehmood and P. Zapol, *Nat. Mater.*, 2009, **8**, 213-216.
10. M. J. Hülsey, B. Zhang, Z. Ma, H. Asakura, D. A. Do, W. Chen, T. Tanaka, P. Zhang, Z. Wu and N. Yan, *Nat. Commun.*, 2019, **10**, 1330.
11. L. Nie, D. Mei, H. Xiong, B. Peng, Z. Ren, X. I. P. Hernandez, A. DeLaRiva, M. Wang, M. H. Engelhard, L. Kovarik, A. K. Datye and Y. Wang, *Science*, 2017, **358**, 1419-1423.
12. C.-T. Kuo, Y. Lu, L. Kovarik, M. Engelhard and A. M. Karim, *ACS Catal.*, 2019, **9**, 11030-11041.
13. S. Zhang, L. Chen, Z. Qi, L. Zhuo, J.-L. Chen, C.-W. Pao, J. Su and G. A. Somorjai, *J. Am. Chem. Soc.*, 2020, **142**, 16533-16537.
14. Y. Lei, F. Mehmood, S. Lee, J. Greeley, B. Lee, S. Seifert, R. E. Winans, J. W. Elam, R. J. Meyer, P. C. Redfern, D. Teschner, R. Schlögl, M. J. Pellin, L. A. Curtiss and S. Vajda, *Science*, 2010, **328**, 224-228.
15. B. T. Qiao, A. Q. Wang, X. F. Yang, L. F. Allard, Z. Jiang, Y. T. Cui, J. Y. Liu, J. Li and T. Zhang, *Nat. Chem.*, 2011, **3**, 634-641.
16. Z. Zhang, Y. Zhu, H. Asakura, B. Zhang, J. Zhang, M. Zhou, Y. Han, T. Tanaka, A. Wang, T. Zhang and N. Yan, *Nat. Commun.*, 2017, **8**, 16100.
17. B. Han, T. Li, J. Zhang, C. Zeng, H. Matsumoto, Y. Su, B. Qiao and T. Zhang, *Chem. Commun.*, 2020, **56**, 4870-4873.
18. Y. Lu, C.-T. Kuo, L. Kovarik, A. S. Hoffman, A. Boubnov, D. M. Driscoll, J. R. Morris, S. R. Bare and A. M. Karim, *J. Catal.*, 2019, **378**, 121-130.
19. Y. B. Lu, J. M. Wang, L. Yu, L. Kovarik, X. W. Zhang, A. S. Hoffman, A. Gallo, S. R. Bare, D. Sokaras, T. Kroll, V. Dagle, H. L. Xin and A. M. Karim, *Nat. Catal.*, 2019, **2**, 149-156.

20. M. Moses-DeBusk, M. Yoon, L. F. Allard, D. R. Mullins, Z. L. Wu, X. F. Yang, G. Veith, G. M. Stocks and C. K. Narula, *J. Am. Chem. Soc.*, 2013, **135**, 12634-12645.
21. K. Ding, A. Gulec, A. M. Johnson, N. M. Schweitzer, G. D. Stucky, L. D. Marks and P. C. Stair, *Science*, 2015, **350**, 189-192.
22. J. Jones, H. F. Xiong, A. T. Delariva, E. J. Peterson, H. Pham, S. R. Challa, G. S. Qi, S. Oh, M. H. Wiebenga, X. I. P. Hernandez, Y. Wang and A. K. Datye, *Science*, 2016, **353**, 150-154.
23. X. I. Pereira-Hernandez, A. DeLaRiva, V. Muravev, D. Kunwar, H. Xiong, B. Sudduth, M. Engelhard, L. Kovarik, E. J. M. Hensen, Y. Wang and A. K. Datye, *Nat. Commun.*, 2019, **10**, 1358.
24. H. L. Guan, J. Lin, B. T. Qiao, X. F. Yang, L. Li, S. Miao, J. Y. Liu, A. G. Wang, X. D. Wang and T. Zhang, *Angew. Chem. Int. Ed.*, 2016, **55**, 2820-2824.
25. W. E. Kaden, T. P. Wu, W. A. Kunkel and S. L. Anderson, *Science*, 2009, **326**, 826-829.
26. A. D. Allian, K. Takanabe, K. L. Fujdala, X. Hao, T. J. Truex, J. Cai, C. Buda, M. Neurock and E. Iglesia, *J. Am. Chem. Soc.*, 2011, **133**, 4498-4517.
27. A. M. Ganzler, M. Casapu, F. Maurer, H. Stormer, D. Gerthsen, G. Ferre, P. Vernaux, B. Bornmann, R. Frahm, V. Murzin, M. Nachtegaal, M. Votsmeier and J. D. Grunwaldt, *ACS Catal.*, 2018, **8**, 4800-4811.
28. A. M. Ganzler, M. Casapu, P. Vernoux, S. Loridant, F. J. C. S. Aires, T. Epicier, B. Betz, R. Hoyer and J. D. Grunwaldt, *Angew. Chem. Int. Ed.*, 2017, **56**, 13078-13082.
29. C. Zong, C. Wang, L. Hu, R. Zhang, P. Jiang, J. Chen, L. Wei and Q. Chen, *Inorg. Chem.*, 2019, **58**, 14238-14243.
30. G. Spezzati, A. D. Benavidez, A. T. DeLaRiva, Y. Su, J. P. Hofmann, S. Asahina, E. J. Olivier, J. H. Neethling, J. T. Miller, A. K. Datye and E. J. M. Hensen, *Appl. Catal. B: Environ.*, 2019, **243**, 36-46.
31. Y. B. Lu, C. Thompson, D. Kunwar, A. K. Datye and A. M. Karim, *ChemCatChem*, 2020, **12**, 1726-1733.
32. S. Oh, H. Ha, H. Choi, C. Jo, J. Cho, H. Choi, R. Ryoo, H. Y. Kim and J. Y. Park, *J. Chem. Phys.*, 2019, **151**, 234716.
33. L. Nie, D. H. Mei, H. F. Xiong, B. Peng, Z. B. Ken, X. I. P. Hernandez, A. DeLariva, M. Wang, M. H. Engelhard, L. Kovarik, A. K. Datye and Y. Wang, *Science*, 2017, **358**, 1419-+.
34. M. J. Hulsey, B. Zhang, Z. Ma, H. Asakura, D. A. Do, W. Chen, T. Tanaka, P. Zhang, Z. Wu and N. Yan, *Nat. Commun.*, 2019, **10**, 1330.
35. Y. Lu, Z. Zhang, F. Lin, H. Wang and Y. Wang, *ChemNanoMat*, 2020, **6**, 1659-1682.
36. Y. Lu, S. Zhou, C.-T. Kuo, D. Kunwar, C. Thompson, A. S. Hoffman, A. Boubnov, S. Lin, A. K. Datye, H. Guo and A. M. Karim, *ACS Catal.*, 2021, **11**, 8701-8715.
37. W. E. Kaden, W. A. Kunkel, M. D. Kane, F. S. Roberts and S. L. Anderson, *J. Am. Chem. Soc.*, 2010, **132**, 13097-13099.
38. W. Huang, J. N. Kuhn, C.-K. Tsung, Y. Zhang, S. E. Habas, P. Yang and G. A. Somorjai, *Nano Lett.*, 2008, **8**, 2027-2034.
39. J. Wang, Y. Lu, L. Liu, L. Yu, C. Yang, M. Delferro, A. S. Hoffman, S. R. Bare, A. M. Karim and H. Xin, *J. Phys. Chem. C*, 2021, **125**, 11380-11390.
40. P. J. Berlowitz, C. H. F. Peden and D. W. Goodman, *J. Phys. Chem.*, 1988, **92**, 5213-5221.
41. H.-H. Liu, Y. Wang, A.-P. Jia, S.-Y. Wang, M.-F. Luo and J.-Q. Lu, *Appl. Surf. Sci.*, 2014, **314**, 725-734.
42. L. DeRita, J. Resasco, S. Dai, A. Boubnov, H. V. Thang, A. S. Hoffman, I. Ro, G. W. Graham, S. R. Bare, G. Pacchioni, X. Q. Pan and P. Christopher, *Nat. Mater.*, 2019, **18**, 746-751.
43. C. R. Yin, F. R. Negreiros, G. Barcaro, A. Beniya, L. Sementa, E. C. Tyo, S. Bartling, K. H. Meiwes-Broer, S. Seifert, H. Hirata, N. Isomura, S. Nigam, C. Majumder, Y. Watanabe, A. Fortunelli and S. Vajda, *J. Mater. Chem. A*, 2017, **5**, 4923-4931.
44. H. V. Thang and G. Pacchioni, *Catal. Lett.*, 2019, **149**, 390-398.
45. G. Che-Galicia, V. Ruíz-Santoyo, R. Zanella, N. Y. Mendoza-González, I. I. Ruiz-López and A. Sampieri, *Chem. Eng. J.*, 2021, **405**, 126644.
46. A. M. Gänzler, M. Casapu, D. E. Doronkin, F. Maurer, P. Lott, P. Glatzel, M. Votsmeier, O. Deutschmann and J.-D. Grunwaldt, *J. Phys. Chem. Lett.*, 2019, **10**, 7698-7705.
47. N. Li, Q.-Y. Chen, L.-F. Luo, W.-X. Huang, M.-F. Luo, G.-S. Hu and J.-Q. Lu, *Appl. Catal. B: Environ.*, 2013, **142-143**, 523-532.
48. M. Cargnello, V. V. T. Doan-Nguyen, T. R. Gordon, R. E. Diaz, E. A. Stach, R. J. Gorte, P. Fornasiero and C. B. Murray, *Science*, 2013, **341**, 771-773.
49. A. M. Karim, C. Howard, B. Roberts, L. Kovarik, L. Zhang, D. L. King and Y. Wang, *Acs Catal.*, 2012, **2**, 2387-2394.
50. B. Ravel and M. Newville, *J. Synchrotron Radiat.*, 2005, **12**, 537-541.
51. M. Newville, *J Synchrotron Radiat.*, 2001, **8**, 322-324.
52. S. Mozaffari, W. H. Li, C. Thompson, S. Ivanov, S. Seifert, B. Lee, L. Kovarik and A. M. Karim, *Nanoscale*, 2017, **9**, 13772-13785.
53. F. Bonet, S. Grugeon, L. Dupont, R. H. Urbina, M. Boudart and G. Djega-Mariadassou, *Kinetics of Heterogeneous Catlytic Reactions*, Princeton University Press / Princeton, N.J., 1984.
54. R. M. Koros and E. J. Nowak, *Chem. Eng. Sci.*, 1967, **22**, 470.
55. R. J. Madon and M. Boudart, *Ind. Eng. Chem. Fund.*, 1982, **21**, 438-447.
56. U. Borštnik, J. VandeVondele, V. Weber and J. Hutter, *Parallel Comput.*, 2014, **40**, 47-58.
57. S. Grimme, S. Ehrlich and L. Goerigk, *J. Comput. Chem.*, 2011, **32**, 1456-1465.
58. J. VandeVondele, M. Krack, F. Mohamed, M. Parrinello, T. Chassaing and J. Hutter, *Comput. Phys. Commun.*, 2005, **167**, 103-128.
59. J. VandeVondele and J. Hutter, *J. Chem. Phys.*, 2003, **118**, 4365-4369.
60. J. Hutter, M. Iannuzzi, F. Schiffmann and J. VandeVondele, *Wiley Interdiscip. Rev. Comput. Mol. Sci.*, 2014, **4**, 15-25.
61. M. Frigo and S. G. Johnson, *Proc. IEEE*, 2005, **93**, 216-231.
62. B. G. Lippert, J. H. Parrinello and Michele, *Mol. Phys.*, 2010, **92**, 477-488.
63. M. Krack, Theor. Chem. Acc., 2005, **114**, 145-152.
64. C. Hartwigsen, S. Goedecker and J. Hutter, *Phys. Rev. B*, 1998, **58**, 3641-3662.
65. J. P. Perdew, K. Burke and M. Ernzerhof, *Phys. Rev. Lett.*, 1997, **77**, 3865.

66. J. Paier, R. Hirschl, M. Marsman and G. Kresse, *J. Chem. Phys.*, 2005, **122**, 234102.
67. J. VandeVondele and J. Hutter, *J. Chem. Phys.*, 2007, **127**, 114105.
68. S. Goedecker, M. Teter and J. Hutter, *Phys. Rev. B*, 1995, **54**, 1703-1710.
69. S. Grimme, J. Antony, S. Ehrlich and H. Krieg, *J. Chem. Phys.*, 2010, **132**, 154104.
70. J. Kolafa, *J. Comput. Chem.*, 2003, **25**, 335-342.
71. W. Tang, E. Sanville and G. Henkelman, *J. Phys. Condens. Matter.*, 2009, **21**, 084204.
72. E. Sanville, S. D. Kenny, R. Smith and G. Henkelman, *J Comput. Chem.*, 2007, **28**, 899-908.
73. G. Henkelman, A. Arnaldsson and H. Jónsson, *Comput. Mater. Sci.*, 2006, **36**, 354-360.
74. M. Yu and D. R. Trinkle, *J. Chem. Phys.*, 2011, **134**, 064111.
75. Q. X. Cai, J. G. Wang, Y. Wang and D. H. Mei, *J. Phys. Chem. C*, 2016, **120**, 19087-19096.
76. M. Tayyem, B. Hamad and B. Paulus, *Chem. Phys.*, 2017, **495**, 10-15.
77. V. Stevanović, Ž. Šljivancanin and A. Baldereschi, *J. Phys. Chem. C*, 2010, **114**, 15653-15660.
78. F. S. Lai and B. C. Gates, *Nano Lett.*, 2001, **1**, 583-587.
79. M. R. Churchill and J. P. Hutchinson, *Inorg. Chem.*, 1978, **17**, 3528-3535.